INTERNATIONAL JOURNAL FOR NUMERICAL AND ANALYTICAL METHODS IN GEOMECHANICS
Int. J. Numer. Anal. Meth. Geomech., **22**, 749–769 (1998)

COUPLED WELLBORE EROSION AND STABILITY ANALYSIS

M. STAVROPOULOU[1], P. PAPANASTASIOU[2,*] AND I. VARDOULAKIS[1]

[1]*Department of Engineering Sciences, National Technical University of Athens, GR-157 73, Athens, Greece*
[2]*Schlumberger Cambridge Research, High Cross, Madingley Road, Cambridge CB3 OEL, U.K.*

SUMMARY

This paper extends earlier work[1] on sand erosion and presents an attempt to couple sand erosion to mechanical damage of rock around a wellbore. Porosity which evolves in time and space as surface erosion progresses, is chosen as the coupling parameter. Both rock elasticity and strength (cohesion) are assumed to depend on porosity in such a way that the material becomes weaker with increasing porosity. The mathematical model, consists of erosion equations, mixture flow equations and stress equilibrium equations, is solved numerically by Galerkin finite element method. Numerical results suggest that erosion, resulting in sand production, is high close to the free surface. Erosion is accompained by changes in porosity and a significant permeability increase. Erosion in the vicinity of the wellbore induces alterations in the mechanical behaviour of the medium. Weakening of rock stiffness leads to severe alteration of both effective stresses and pore pressure near the cavity. Since cohesion decreases with increasing porosity, one can also identify the time instant at which rock mechanical failure starts. © 1998 John Wiley & Sons, Ltd.

Key words: wellbore stability; sand erosion; sand production; sand prediction; radial flow; poroelasticity

1. INTRODUCTION

Wellbore instabilities and production of solids (mainly sand) are common problems in oil producing wells embedded in formations that are inherently weak. Sand prediction models aim at optimizing fluid production rates while avoiding near-wellbore instabilities and damage of reservoir structure. The prediction of sand production is essential to the decision whether sand control techniques will require to be installed during the well completion phase. The high completion cost and the reduction of well productivity which are associated with sand control measures, especially in the case of gravel packing, make sand prediction models a valuable tool.

The different processes involved in sand production are associated with fluid and solids movement, fluid/rock interaction and rock deformation. From the modelling point of view, sand production is usually related to the following two failure mechanisms: (1) mechanical instabilities and localized failure (damage) of the rock in the vicinity of the wellbore due to stress

*Correspondence to: P. Papanastasiou, Schlumberger Cambridge Research, High Cross, Madingley Road, Cambridge CB3 OEL, U.K.

CCC 0363–9601/98/090749–21$17.50

Received 7 March 1997
Revised 12 December 1997

concentration[2] and (2) hydro-mechanical instabilities due to internal and surface erosion, which manifest themselves in releasing and displacing of particles, caused by the action of seepage forces. The mechanical failure and erosion mechanisms are coupled to one another, since stress concentrations lead to localized damage, which in turn increases the amount of loose particles that can leave the matrix and enter the population of particles in transport. On the other hand, washing-out of particles increases the porosity of the intact rock and may cause re-adjustment of the intergranular forces leading to further strength decrease and damage of the rock.

All the existing sand prediction models treat the problem similar to the wellbore stability addressing only the problem of sand initiation, see, for example, References 3 and 4. The first work considering sand production as an erosion phenomenon was reported recently in a paper by the authors.[1] The paper examined the hydro-mechanical aspect of the sand production problem and set the basic frame of a mathematical model. Surface erosion and piping effects were studied on the basis of mass balance and particle transport considerations as well as Darcy's law. In the first model, all deformation and strength characteristics of the rock were suppressed assuming a cohesionless material similar to loose sand, and the emphasis was put on mass transport. The paper considered Darcy flow normal to the free surface of an inhomogeneous half-space with permeability which depends on the porosity. The results showed that surface erosion is accompained by high changes of porosity and permeability close to the free surface. The paper suggested that quantities which can be measured in experiment, like the amount of produced soils or fluid discharge, can be used in an inverse way to determine the constitutive parameters of the problem. We emphasize here that the experimental studies of sand production given more qualitative than quantitative information on the erosion phenomenon [5]. The shortage of quantitative experimental data may partly be attributed to the lack of theoretical framework which could guide the design of basic sand erosion experiments.

This study extends our previous work[1] and presents an attempt to couple sand erosion to mechanical damage of rock around a wellbore. We considered a wellbore in a deep rock formation as illustrated in Figure 1. The fluid flow is considered to be radial (towards the free surface of the wellbore). Also radial symmetry around the well axis is assumed. Under these conditions any deformation of the rock will take place in a plane normal to the borehole axis. The rock is treated as a porous and permeable material and erosion is mainly governed by the possibility of grains passing through the interconnected void space and the existence of defects as erosion starters points.

The studied approach is based on a three-phase mixture theory for a continuum consisting of skeleton solids, fluidized-solids and fluid.[1] The formulation of the differential equations pertaining to the erosion kinematics is superseded by the numerical solution based on Galerkin finite element scheme. Accordingly, an approximate solution is obtained assuming that the velocity of the fluid flow is much greater than the deformation rate of the solid skeleton. The solids skeleton is deformed only due to variation of the stress field. Further on, a theory of partial stresses is developed and the stress equilibrium equations, as well as the constitutive relations of a poroelastic medium are presented. Porosity which evolves in time and space as surface erosion progresses is chosen as a coupling parameter. Both rock elasticity and strength (cohesion) are assumed to depend on porosity in such a way that the material becomes weaker with increasing porosity. Combining the above relationships a single non-linear differential equation which describes the radial displacement is obtained. This equation is solved numerically at each time step using a second Galerkin finite element scheme. Finally, based on the derived stress solution

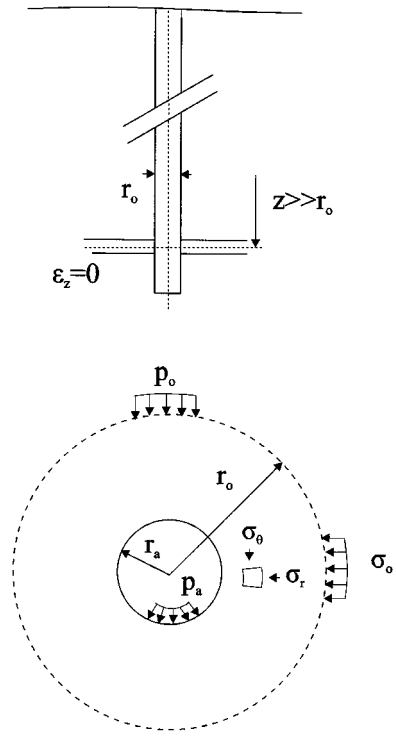

Figure 1. Configuration of the problem

around the circular opening, a stability analysis is performed using a modified Mohr–Coulomb failure criterion expressed in terms of Terzaghi principal effective stresses. The degradation of the medium is described by a simple damage law according to which the diminution of the cohesion is quantiatively proportional to the porosity. Since cohesion decreases with increasing porosity, one can identify the time instant at which the rock starts failing and producing sand.

2. DEFINITION OF BASIC HYDRO-MECHANICAL EQUATIONS

2.1. Mass balance and particle transport

The saturated porous medium is modelled as a three-phase system consisting of skeleton solids (s), fluidized-solids (fs) and fluid (f).[1] Fluidized particles are particles in suspension that move with the fluid. Any other loose particles which are trapped inside the void space are seen as part of the solid phase. Moreover, it is assumed that fluid and fluidized particles share at any instant the same velocity. The solid is assumed to be rigid. In other words, a solid particle has either zero velocity and is assigned to the solid phase or has the velocity of the fluid and is assigned to the mixture which fills the void space. The volume fraction of voids is expressed by the

bulk porosity ϕ

$$\phi = \frac{\mathrm{d}V_\mathrm{v}}{\mathrm{d}V} \tag{1}$$

where $\mathrm{d}V$ indicates a volume element and $\mathrm{d}V_\mathrm{v}$ is the volume of interconnected void space of pores which is fully occupied by the mixture of fluid and fluidized particles. The transport concentration of the fluidized solids c is defined by

$$c = \frac{\mathrm{d}V_\mathrm{fs}}{\mathrm{d}V_\mathrm{v}} \tag{2}$$

where $\mathrm{d}V_\mathrm{fs}$ indicates the volume of fluidized particles. It should be noticed that ϕ and c are functions of location and time. The partial densities of the solid phase (index 1) and the mixture phase (index 2) coincide with the bulk densities of the corresponding constituents

$$\rho^{(1)} = \frac{\mathrm{d}M_\mathrm{s}}{\mathrm{d}V} = (1-\phi)\rho_\mathrm{s} \tag{3}$$

$$\rho^{(2)} = \frac{\mathrm{d}\bar{M}}{\mathrm{d}V} = \frac{\mathrm{d}M_\mathrm{f} + \mathrm{d}M_\mathrm{fs}}{\mathrm{d}V} = \phi\bar{\rho} \qquad \bar{\rho} = c\rho_\mathrm{s} + (1-c)\rho_\mathrm{f} \tag{4}$$

where $\mathrm{d}M_\mathrm{s}$ is the mass of solids, $\mathrm{d}M_\mathrm{f}$ is the mass of fluid phase, $\mathrm{d}M_\mathrm{fs}$ is the mass of fluidized-particles, $\mathrm{d}\bar{M}$ is the mass of mixture, ρ_s is the density of solids, ρ_f is the density of fluid and $\bar{\rho}$ is the density of mixture. The volume discharge rate of the mixture is defined by the relation

$$\bar{q}_i = \frac{\mathrm{d}\bar{V}}{\mathrm{d}S_i\,\mathrm{d}t} \tag{5}$$

where $\mathrm{d}\bar{V}$ is the volume of flow through the cross-sectional area $\mathrm{d}S_i$ in time $\mathrm{d}t$.

Mass balances for the solid phase, fluidized particles and fluid phase are given by the following expression:[1]

$$\frac{\partial\phi}{\partial t} = \frac{\dot{m}}{\rho_\mathrm{s}} \tag{6}$$

$$\frac{\partial c\phi}{\partial t} + \mathrm{div}(c\bar{q}_i) = \frac{\dot{m}}{\rho_\mathrm{s}} \tag{7}$$

$$\mathrm{div}\,\bar{q}_i = 0 \tag{8}$$

where $\dot{m}$ is a mass generation term, which corresponds to the rate of net mass eroded and fluidized at any time and point. Notice that in this study the hydro-mechanical dispersion is disregarded. Equations (6)–(8) constitute the set of mass balance equations for the considered problem. These equations do not suffice for solving the problem since a constitutive relation for the mass generation term is needed. A constitutive law for the rate of eroded mass, suggesting that erosion is driven by the discharge of the fluidized particles cq_i, is given by the following relation:[6,7,1]

$$\frac{\dot{m}}{\rho_\mathrm{s}} = \lambda(1-\phi)\left(c - \frac{c^2}{c_\mathrm{cr}}\right)|\bar{q}_i| \tag{9}$$

where c_{cr} is a critical value of c for which the two competing phenomena, erosion and deposition (plugging) balance each other. The coefficient λ has dimension of inverse length, $[\lambda] = L^{-1}$, and is probably related to the spatial frequency of the potential erosion starters points in the solid skeleton of the porous medium and must be determined experimentally. In case of coupling between erosion process and rock weakening, λ is expected to be an increasing function of rock damage.

2.2. *Stresses, partial stresses, damage*

For the formulation of stress–strain relationships the concept of partial stress in a mixture theory is utilized. The medium is treated as a two-phase mixture equipped by a total (Cauchy) stress tensor σ_{ij} and by partial stresses $\sigma_{ij}^{(a)}$ which are assigned to the solid phase ($a = 1$) and fluid phase ($a = 2$).[8] The total stress is the summation of the partial stresses

$$\sigma_{ij} = \sigma_{ij}^{(i)} + \sigma_{ij}^{(2)} \tag{10}$$

The partial stress for the fluid phase is directly related to the pore fluid pressure p, via

$$\sigma_{ij}^{(2)} = -\phi p \delta_{ij} \tag{11}$$

and the partial stress for the solid phase is given by

$$\sigma_{ij}^{(1)} = (1 - \phi)\bar{\sigma}_{ij} \tag{12}$$

where $\bar{\sigma}_{ij}$ is the constitutive part that is related to the strains. Here we adopt the simplest possible model; i.e. an isotropic linear elastic model

$$\bar{\sigma}_{ij} = 2G\varepsilon_{ij} + \Lambda\varepsilon_{kk}\delta_{ij} \tag{13}$$

where Λ and G are the Lame's parameters, given below in terms of the Poisson's ratio, v, and the Young's modulus, $\bar{E}$,

$$\Lambda = \frac{\bar{E}v}{(1 - v)(1 - 2v)}, \qquad G = \frac{\bar{E}}{2(1 - v)} \tag{14}$$

We notice that combination of equations (12) and (13) leads to a poroelastic model with internal damage and with porosity, $0 < \phi < 1$, being the damage parameter[9]

$$E = \bar{E}(1 - \phi) \tag{15}$$

It should be noticed that in this analysis the total porosity and the porosity of the interconnected void space are assumed to be the same, having in mind a material like a porous sandstone.

According to Terzaghi's effective stress principle the total stress is decomposed into an effective stress, assigned to the soil skeleton, and into a pore fluid pressure

$$\sigma_{ij} = \sigma'_{ij} - p\delta_{ij} \tag{16}$$

We notice that based on experimental evidence, strength criteria are formulated in terms of Terzaghi's effective stress. Combining equations (10)–(12) and (16) the relation between the

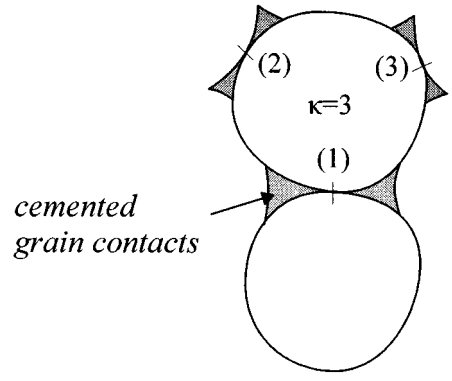

Figure 2. Coordination number

Terzaghi's effective stress σ'_{ij}, the constitutive stress, $\bar{\sigma}_{ij}$, and the pore water pressure, p, can be derived

$$\sigma'_{ij} = (1 - \phi)[\bar{\sigma}_{ij} + p\delta_{ij}] \tag{17}$$

Erosion phenomena in turn, cause the degradation of the granular medium through porosity increase and diminution of the cohesion between the grains. The parameter that describes the number of grains in contact is the coordination number, k, Rumpf.[8] The coordination number is inversely proportional to porosity of the medium (Figure 2). Considering Rumpf's observation, in the present analysis the degradation of the medium is described by a simple damage law according to which the diminution of the cohesion C is quantitatively proportional to the porosity[10]

$$C = \bar{C}(1 - \phi) \tag{18}$$

Taking into account relation (18), the Mohr–Coulomb failure criterion, expressed in terms of principal effective stresses, is modified as follows:[11]

$$\tfrac{1}{2}(\sigma'_1 + \sigma'_2)\sin\Phi - \tfrac{1}{2}(\sigma'_1 - \sigma'_2) = C\cos\Phi = \bar{C}(1 - \phi)\cos\Phi \tag{19}$$

or

$$t_m = -q_m \sin\Phi + C\cos\Phi \tag{20}$$

where Φ is the rock friction angle, t_m is the shear stress and q_m is the mean pressure.

3. COUPLED WELLBORE STABILITY ANALYSIS

3.1. Wellbore erosion

Combining equation (6) with equations (7) and (9) and taking into account the continuity equation (8) the formulation of the axisymmetric erosion kinetics is obtained

$$\frac{\partial(c\phi)}{\partial t} + \bar{q}_{\mathrm{r}}\frac{\partial c}{\partial r} = \frac{\partial \phi}{\partial t} \tag{21}$$

$$\frac{\partial \phi}{\partial t} = \lambda(1 - \phi)\left(c - \frac{c^2}{c_{\mathrm{cr}}}\right)|\bar{q}_{\mathrm{r}}| \tag{22}$$

On the other hand, flow in a porous medium is governed by Darcy's law which says that the flow rate or mixture discharge q_r is driven by the gradient of pore fluid pressure

$$\bar{q}_r = -\frac{k}{\eta_k \bar{\rho}} \frac{\partial p}{\partial r}, \quad \bar{q}_r = -q > 0 \tag{23}$$

where η_k is the kinematic viscosity of the fluid, p is the pore fluid pressure and $\bar{\rho}$ is the partial density of the mixture defined in equation (4).

We recall that the physical permeability k of a porous medium in general depends on porosity ϕ. For example, the Carman–Kozeny equation,[12,8] gives

$$k = k_0 \frac{\phi^3}{(1-\phi)^2} \tag{24}$$

The physical permeability k has the dimensions of surface, which means that k stands as a measure of the cross-sectional area of the microscopic channels in the interconnected void space. The physical permeability k is usually measured in millidarcy ($1\ \text{md} = 0{\cdot}987 \times 10^{-15}\,\text{m}^2$).

Substituting $\bar{q}_r$ from Darcy's law (23), in continuity equation (8), the following expression is obtained:

$$\frac{\partial^2 p}{\partial r^2} + \frac{\partial p}{\partial r}\left[\frac{1}{r} + \alpha \frac{\partial \phi}{\partial r} + \beta \frac{\partial c}{\partial r}\right] = 0 \tag{25}$$

where α and β are in general functions of c and ϕ. Here due to the assumptions made in (23) and (24)

$$\alpha = \frac{3-\phi}{\phi(1-\phi)}, \qquad \beta = -\frac{\rho_s - \rho_f}{(1-c)\rho_f + c\rho_s} \tag{26}$$

The system of equations to be solved simultaneously consists of:

(a) mass balance equation (21) and evolution law for porosity (22) which both govern the erosion process,
(b) Darcy's law (23) with the appropriate definitions for partial density (4) and permeability (24) and
(c) continuity equation (25) which models the flow of the mixture.

The coupled non-linear governing differential equations with unknowns ϕ, c, q and p are supplemented with the following boundary conditions at the remote boundary r_0 and at the wellbore surface r_a,

$$c(r_0, t) = c_0, \qquad p(r_0, t) = p_0, \qquad p(r_a, t) = p_a$$

For simplicity the initial porosity and transport concentration are assumed to be constant

$$\phi(r, 0) = \phi_0, \qquad c(r, 0) = c_0)$$

The initial profiles for flow rate and pore pressure are determined from Darcy's law assuming a homogeneous medium. However, it should be noticed that other initial and boundary

conditions for ϕ and c are also possible which may lead to smooth or non-smooth solutions due to the hyperbolic character of equation (21).

3.2. *Wellbore stresses, deformation and failure*

For the problem considered, a plane-strain axially symmetric deformation analysis is performed. Taking into account equations (10)–(14), the elastic constitutive relations between total stress and total strain can be derived from

$$\sigma_{\mathrm{r}} = \frac{\bar{E}(1-\phi)}{(1+\nu)(1-2\nu)}\left[(1-\nu)\varepsilon_{\mathrm{r}} + \nu\varepsilon_{\theta}\right] - \phi p \tag{27}$$

$$\sigma_{\theta} = \frac{\bar{E}(1-\phi)}{(1+\nu)(1-2\nu)}\left[(1-\nu)\varepsilon_{\theta} + \nu\varepsilon_{\mathrm{r}}\right] - \phi p \tag{28}$$

For the considered axisymmetric plane–strain conditions the corresponding strains are expressed in terms of the radial displacement $u_{\mathrm{r}} = u(r, t)$ only

$$\varepsilon_{\mathrm{r}} = \frac{\partial \mathrm{u}}{\partial r} \tag{29}$$

$$\varepsilon_{\theta} = \frac{u}{r} \tag{30}$$

The equation of stress equilibrium for $\sigma_{\mathrm{r}} = \sigma_{\mathrm{r}}(r, t)$ and $\sigma_{\theta} = \sigma_{\phi}(r, t)$, neglecting body forces, takes the form

$$\frac{\partial \sigma_{\mathrm{r}}}{\partial r} + \frac{\sigma_{\mathrm{r}} - \sigma_{\theta}}{r} = 0 \tag{31}$$

Substituting equations (27)–(30) into equilibrium equation (31), the following differential equation describing the radial displacement appears:

$$\frac{\partial^2 u}{\partial r^2} + g_1 \frac{\partial u}{\partial r} - g_2 u = g_3 \frac{\partial(\phi p)}{\partial r} \tag{32}$$

where $g_i = g_i(r, t)$ are functions of ν and $\phi = \phi(r, t)$ which are given in Appendix II.

For the open hole of Figure 1 the stress boundary conditions are

$$\sigma_{\mathrm{r}}(r_a, t) = -p_a, \qquad \sigma_{\mathrm{r}}(r_0, t) = -\sigma_0$$

which in terms of displacement u become

$$\left.\frac{\partial u}{\partial r}\right|_{r=r_a} = -\frac{\nu}{1-\nu}\frac{u(r_a)}{r_a} - g_3(r_a, t)\left[\phi(r_a, t)p_a - p_a\right] \tag{33}$$

$$\left.\frac{\partial u}{\partial r}\right|_{r=r_0} = -\frac{\nu}{1-\nu}\frac{u(r_0)}{r_0} + g_3(r_0, t)\left[\phi_0 p_0 - \sigma_0\right] \tag{34}$$

The radial displacement, u, can be obtained solving numerically the partial differential equation (32) with boundary conditions (33) and (34). Once u and $\partial u/\partial r$ are determined, the stress solution can be derived by introducing the result into equations (27) and (28).

4. NUMERICAL SOLUTION

The system of governing equations of erosion kinetics (21)–(23) and (25) is solved numerically by a discretization procedure using the Galerkin finite element method in space and finite differences in time. The first step of this scheme is to discretize the space domain replacing the original set of PDE with a set of ODE and then to apply a second discretization in time alone. Considering the non-linearity of equation system, the solution is obtained with Newton's method. The system can be put in a compact form:

$$R(\phi, c, q, p) = 0 \tag{35}$$

where R is the vector of residuals. Newton's method is an iterative method where, given an initial approximation $y(0)$ to the solution y, the $(m+1)$th approximation is obtained from the mth by solving

$$J(y(m))[y_{(m+1)} - y_{(m)}] = -R(y_{(m)}) \tag{36}$$

where J is the Jacobian matrix which contains the partial derivatives of the residuals R with respect to the unknowns, i.e. $J_{ij} = (\partial R^i/\partial y_j)$. The derivatives are evaluated at $y = y_{(m)}$. The integer m is the iteration counter. Time discretization is accomplished through a fully explicit finite difference scheme using the following two approximations. They are derived from Taylor series expansions and denote evaluation of a quantity y and its time derivative $\mathrm{d}y/\mathrm{d}t$ at time $t = t_n + \theta\Delta t$ which falls in the time interval $\Delta t = t_{n+1} - t_n$

$$y^{n+\theta} \approx (1-\alpha)y^n + \alpha y^{n+1} \qquad \left.\frac{\mathrm{d}y}{\mathrm{d}t}\right|_{n+\alpha} \approx \frac{y^{n+1} - y^n}{\Delta t} \tag{37}$$

The unknown variables are expressed in terms of their nodal values as

$$\phi = \sum_{j=1}^{N} \phi_j \Phi^j \quad c = \sum_{j=1}^{N} c_j \Phi^j \quad q = \sum_{j=1}^{N} q_j \Phi^j \quad p = \sum_{j=1}^{N} p_j \Phi^j \tag{38}$$

where Φ^j are the approximation functions (basis functions) over the element. For these approximations the Lagrange quadratic interpolation functions were used.

The Galerkin-weighted residuals of the system equations are formed by multiplying them by each basis function Φ^i in turn and then integrating over the entire space-domain $[r_a, r_0]$. At each step of Newton's iteration equation (36) can be written in an expanded form

$$\begin{vmatrix} \partial R_i^1/\partial\phi & \partial R_i^1/\partial c & \partial R_i^1/\partial q & 0 \\ \partial R_i^2/\partial\phi & \partial R_i^2/\partial c & \partial R_i^2/\partial q & 0 \\ \partial R_i^3/\partial\phi & \partial R_i^3/\partial c & \partial R_i^3/\partial q & \partial R_i^3/\partial p \\ \partial R_i^4/\partial\phi & \partial R_i^4/\partial c & 0 & \partial R_i^4/\partial p \end{vmatrix}^m \begin{vmatrix} \delta\phi \\ \delta c \\ \delta q \\ \delta p \end{vmatrix}^{(m+1)} = - \begin{vmatrix} R_i^1 \\ R_i^2 \\ R_i^3 \\ R_i^4 \end{vmatrix}^m \tag{39}$$

The derivation of Galerkin-weighted residuals R_i^j and their partial derivatives $J_{ij} = (\partial R^i/\partial y_j)$ which form the elements of the Jacobian matrix is given in the Appendix I. The set of linear equations (39) can be solved repeatedly until the iteration converges to the solution ($y = \phi, c, q, p$) of the equation set (35). Convergence is achieved when the Eucledian norm of the solution update, δy, approximately vanishes.

In parallel, since the values of variables ϕ, c, q and p at every node and at each time step were calculated, the partial differential equation (32) can be solved at each time step by employing a second Galerkin finite element scheme. The unknowns of the second numerical scheme are the value of the function u and its first derivative, $\partial u/\partial r$, at the nodal points. The solution is approximated by the expression

$$u = \sum_{j=1}^{N} u_j \Phi^j \tag{40}$$

where the basis functions Φ^j here are Hermite cubic polynomials. This leads to two double nodes/element with two basis functions for interpolating the function u and other two for interpolating the slope $\partial u/\partial r$.

Equation (32) with boundary conditions (33) and (34) can be assembled in matrix form as follows:

$$[a]\{u\} = \{b\} \tag{41}$$

The elements of matrix $[a]$ and vector $\{b\}$ are derived from the Galerkin form of equation (32) and they are given in Appendix II.

Finally, a non-uniform mesh with element length increasing according to a simple geometric law is used for the spatial discretization.

5. NUMERICAL RESULTS AND DISCUSSION

Computational results for the coupled wellbore erosion and stability analysis problem will be presented for the set of parameters shown in Table I. With these data the process starts at time $t = 0$ from a Darcy flow. The time factor is described by the flow rate which governs the time evolution of porosity and consequently the lifetime of the wellbore.

The time history and the spatial profiles at different time steps of the varying properties are shown in Figures 3–12. Figure 3 shows that the alteration of porosity is high close to the free surface and it diminishes rapidly within a small distance from it. This indicates that the erosion process is more active close to the free surface. Such a porosity distribution results in permeability inhomogeneity, according to the Carman–Kozeny equation (24), which in turn results in lower pressure gradients in the eroded region (Figure 4). For the same reason the pore pressure at $r = 1{\cdot}0$ m is relatively low (Figure 4) although the porosity at this radius has not increased far beyond its initial value (Figure 3). As we can see, the original logarithmic pressure profile for the axisymmetric problem considered is convex and as time progresses the curvature changes in the opposite direction yielding a concave profile. The next plots, Figures 5 and 6 depict the time history of porosity and transport concentration at the free surface of the wellbore. The results show that porosity and transport concentration increase rapidly (after the elapsed of some time) in the beginning and as time progresses the rate drops. The transport concentration in

Table I. Input parameters of computational example

Wellbore radius	$r_a = 0{\cdot}1$ m
Outer boundary radius	$r_0 = 5$ m
Initial porosity	$\phi(r, 0) = \phi_0 = 0{\cdot}25$
Initial transport concentration	$c(r, 0) = c_0 = 10^{-3}$
Critical transport concentration	$c_{cr} = 0{\cdot}3$
Initial permeability	$k(r, 0) = k_0(\phi_0^3/(1-\phi_0)^2) = 373$ md
Initial Young's modulus	$E = 2$ GPa
Poisson's ratio	$v = 0{\cdot}3$
Kinematic viscosity of the fluid	$\eta_k = 5 \times 10^{-6}\,\mathrm{m^2\,s^{-1}}$
Density of fluid	$\rho_f = 840\,\mathrm{kg\,m^{-3}}$
Density of solids	$\rho_s = 2650\,\mathrm{kg\,m^{-3}}$
Wellbore fluid pressure	$p(r_a, t) = 5$ MPa
Far field pore pressure	$p(r_0, t) = 8$ MPa
Uniform exterior stress	$\sigma_0 = 20$ MPa
Frequency	$\lambda = 5\,\mathrm{m^{-1}}$

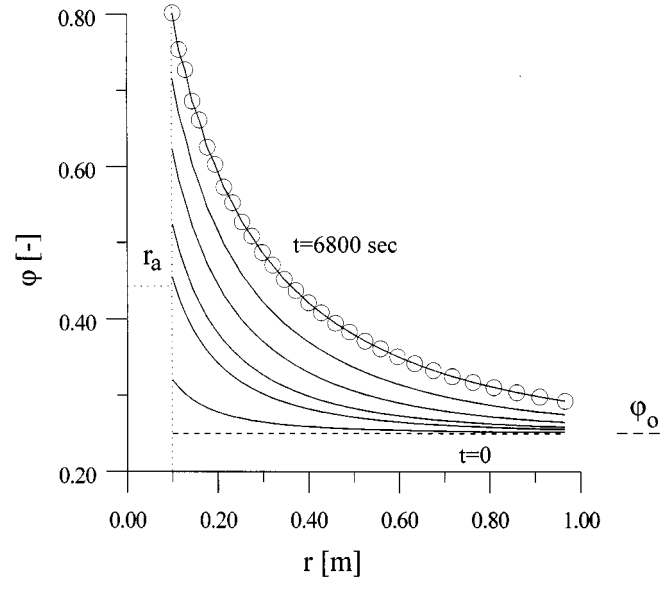

Figure 3. Spatial profiles of porosity at various time steps

Figure 6 would eventually converge to the asymptotic value $c_{cr} = 0{\cdot}3$. Figure 7 depicts the time history of flow rate. The flow rate increases as time progresses and finally approaches infinity as the permeability of the medium becomes very large.

Furthermore, erosion in the vicinity of the wellbore induce alterations in the mechanical behaviour of the medium (Figures 8–12). Figure 8 shows the spatial profiles of radial displacement

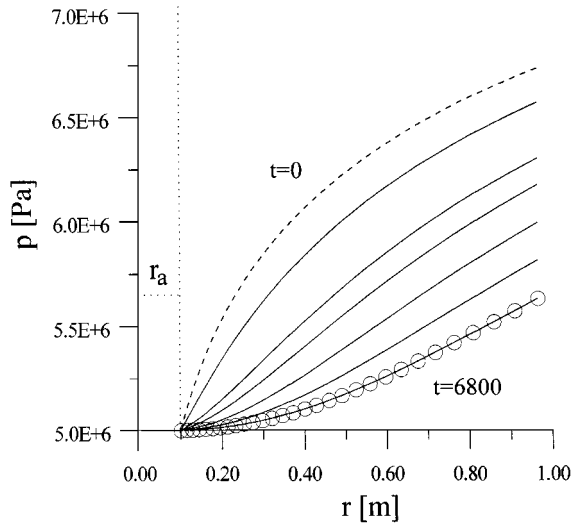

Figure 4. Spatial profiles of pore pressure at various time steps

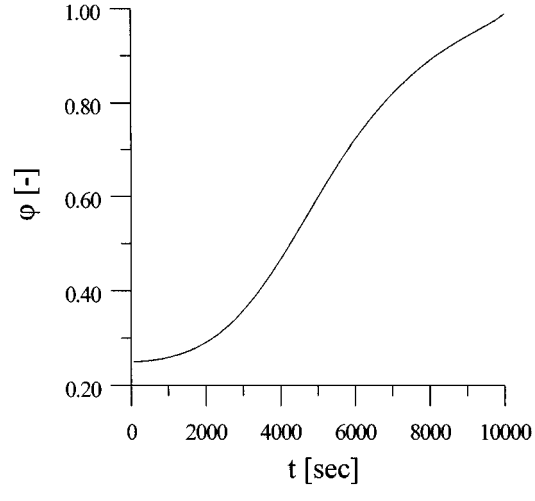

Figure 5. Time variation of porosity at free surface, $r = r_a$

at various time steps and Figure 9 demonstrates the variation with time of radial displacement and its slope at the wellbore surface. From those two diagrams, we can observe that the absolute value of the radial displacement and its slope increase with time. These increases cause in turn a decrease in the gradient of the effective radial stress (Figure 10), and at the same time a decrease in the value of the effective tangential (or hoop) stress (Figure 11). The curves $t = 6800$ in Figures 3 and 4 have twice as many circles as Figures 8, 10 and 11 due to the two different levels of mesh

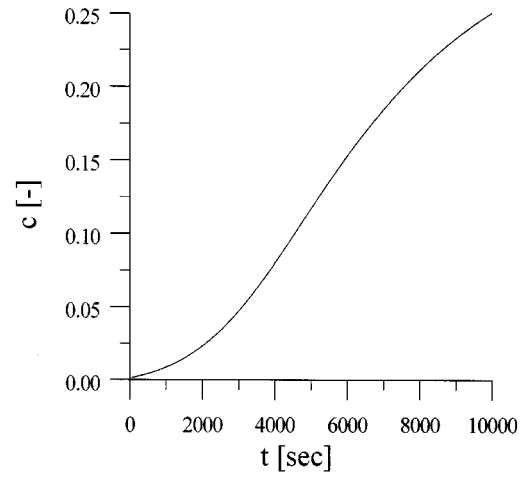

Figure 6. Time variation of transport concentration at free surface, $r = r_a$

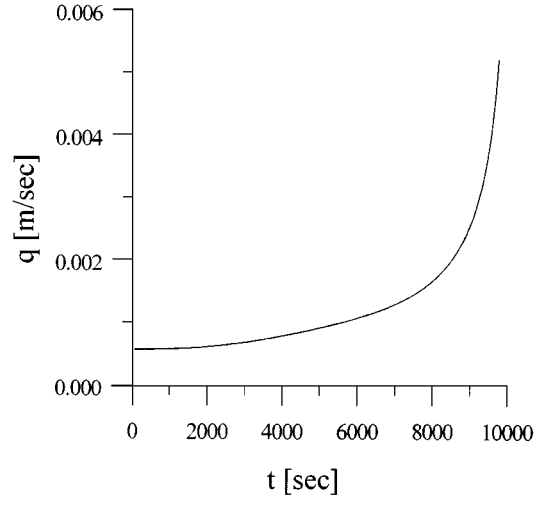

Figure 7. Time variation of flow rate at free surface, $r = r_a$

discretization. Figure 11 shows that the gradient of the effective tangential stress decreases monotonically until it reaches the value of zero and then it changes sign and it increases. Such a stress distribution in the vicinity of the wellbore results in a decrease of the stress concentration factor

$$K = \frac{\sigma'_\theta}{-\sigma_0 + p_a} \tag{42}$$

at the free boundary of the hole as time evolves (Figure 12).

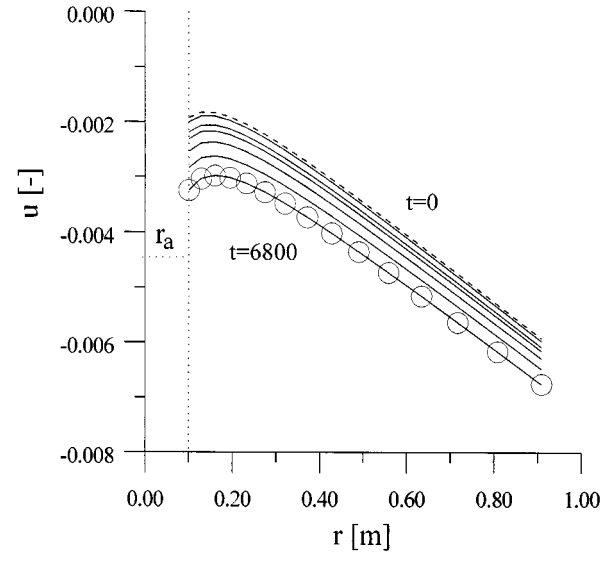

Figure 8. Distribution of radial displacement at various time steps

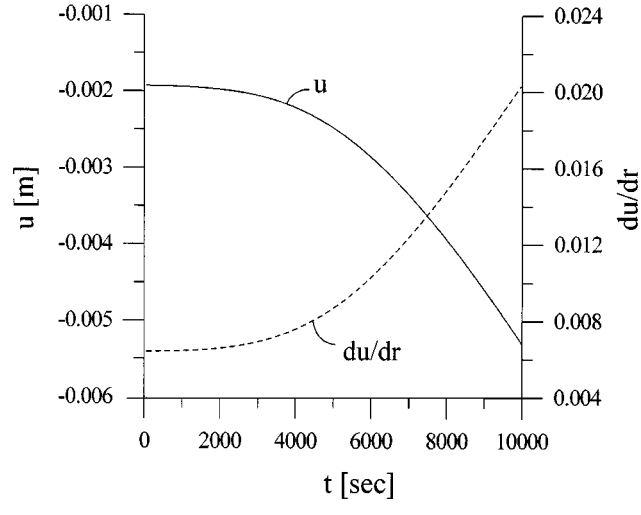

Figure 9. Time variation of radial displacement and its slope at the wellbore surface, $r = r_a$

Considering the solution of the elastic stress boundary value problem, a failure analysis of the borehole was carried out using a modified Mohr–Coulomb criterion (19). In the present analysis, the cohesion is related to the damage of the medium through a conceptual cohesion–softening model (Figure 13). The results are demonstrated in Figures 14 and 15. The shrinkage of the failure

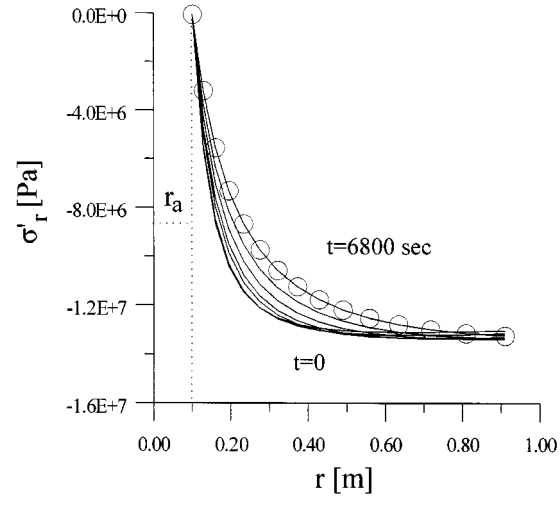

Figure 10. Distribution of radial effective stress at various time steps

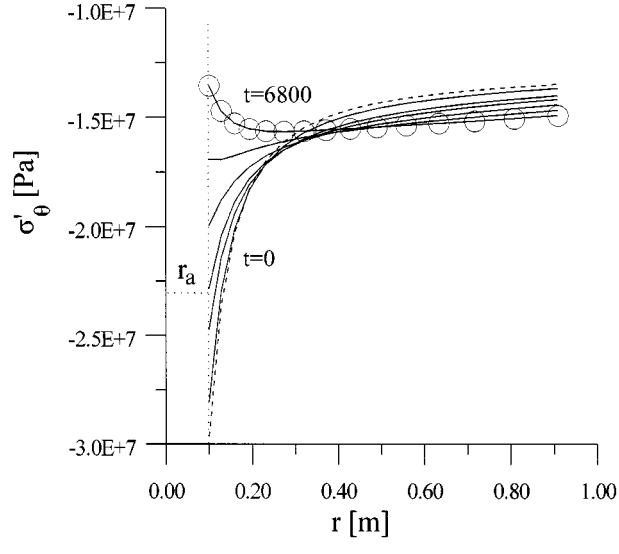

Figure 11. Distribution of tangential effective stress at various time steps

envelope and at the same time the decrease of shear stress is shown in Figure 14. This shrinkage effect is due to the decrease of the cohesion of the medium whereas the decrease of shear stress is caused by the relief of the stress concentration in the eroded regions around the hole. After the elapse of 3300 s, the decrease of the shear strength (cohesion) at the borehole wall is greater than the decrease of the shear stress and collapse of the rock formation is anticipated. This is shown

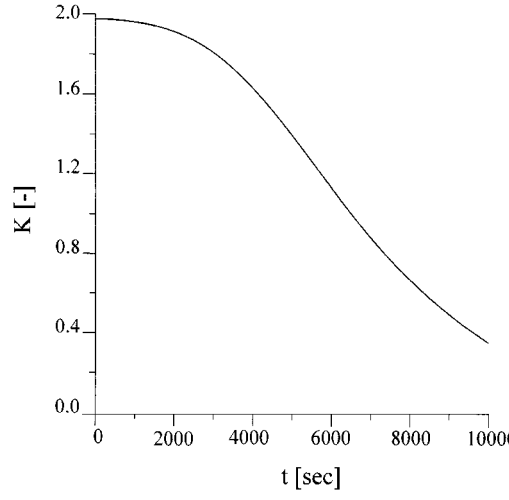

Figure 12. Time variation of the stress concentration factor at the wellbore surface $r = r_a$

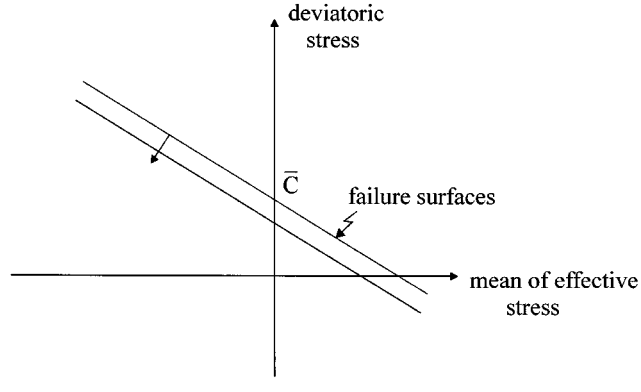

Figure 13. Conceptual cohesion-softening model, $C = \bar{C}(1 - \phi)$

more clearly in Figure 15 where the time variation of the failure envelope and the stress field at the free boundary of the wellbore is plotted. The present analysis can be easily extended to account for elastoplastic deformation. In such a case the stress state will remain on the yield surface which shrinks with increasing porosity until a critical condition for failure is met.

6. CONCLUSIONS

This paper presents a way of coupling sand erosion to mechanical damage of rock near a wellbore. Porosity which evolves in time and space, as surface erosion progresses, is chosen as the coupling parameter. Both rock elasticity and strength (cohesion) are assumed to depend on

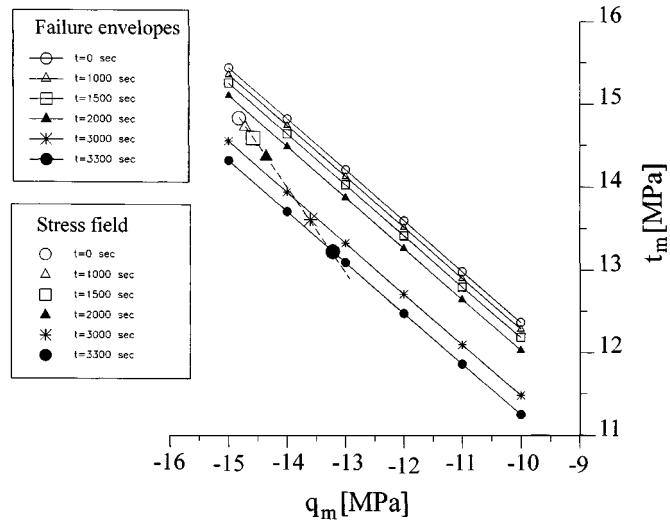

Figure 14. Failure envelopes and corresponding critical stresses at the free boundary of the wellbore, $r = r_a$, at various time steps ($\Phi = 37°$, $\bar{C} = 7{\cdot}5$ MPa)

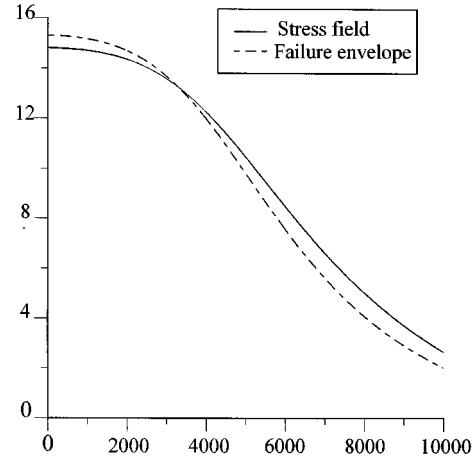

Figure 15. Time variation of the failure envelope and the stress field at the free boundary of the wellbore, $r = r_a$, ($\Phi = 37°$, $\bar{C} = 7{\cdot}5$ MPa)

porosity in such a way that the material becomes weaker with increasing porosity. The time factor is described by the flow rate which governs the time evolution of porosity and consequently the lifetime of the wellbore. The mathematical model, consists of erosion equations, mixture flow equations and stress equilibrium equations, is solved numerically by Galerkin finite element method. Based on the numerical results the following conclusions are drawn:

(1) Erosion is high close to the free surface and decays rapidly with short distance from it. The erosion near to the free surface is accompained by changes in porosity and a significant

permeability increase. Inhomogeneity in permeability results in different pressure profiles as time progresses with lower pressure gradients in the eroded regions.

(2) Erosion in the vicinity of the wellbore induces alterations in the mechanical behaviour of the medium. The mechanical damage causes reduction of the stress concentration factor in this region. Furthermore, the increase of porosity results in reduction of cohesion between the grains and shrinkage of the failure envelope. Since cohesion decreases with increasing porosity, the time instant at which rock starts failing and producing sand can be identified.

APPENDIX I

Discretization of the governing hydromechanical equations

The Galerkin-weighted residuals of the governing differential equations of erosion kinetics (21)–(23) are given by[13]

$$R_i^1 = \int_{r_a}^{r_0} \left[\frac{(c\phi)^{n+1} - (c\phi)^n}{\Delta t} - aq^{n+1} \left[\frac{\partial c}{\partial r} \right]^{n+1} - (1-a) q^n \left[\frac{\partial c}{\partial r} \right]^n - \frac{\phi^{n+1} - \phi^n}{\Delta t} \right] \Phi^i \, \mathrm{d}r \tag{43}$$

$$R_i^2 = \int_{r_a}^{r_0} \left[\frac{\phi^{n+1} - \phi^n}{\Delta t} - a\lambda'(1-\phi^{n+1}) \left(c^{n+1} - \frac{c^{(n+1)^2}}{c_{\mathrm{cr}}} \right) q^{n+1} - (1-a)\lambda'(1-\phi^n) \times \left(c^n - \frac{c^{n^2}}{c_{\mathrm{cr}}} \right) q^n \right] \Phi^i \, \mathrm{d}r \tag{44}$$

$$R_i^3 = \int_{r_a}^{r_0} \left[a \left[\frac{\partial p}{\partial r} \right]^{n+1} + (1-a) \left[\frac{\partial p}{\partial r} \right]^n - a \frac{\eta_{\mathrm{k}}}{k_0} \frac{(1-\phi^{n+1})^2}{\phi^{n+1^3}} \rho^{-n+1} q^{n+1} - (1-a) \times \frac{\eta_{\mathrm{k}}}{k_0} \frac{(1-\phi^n)^2}{\phi^{n^3}} \rho^{-n} q^n \right] \Phi^i \, \mathrm{d}r \tag{45}$$

In order to derive the residual of equation (25) and to utilize the appropriate boundary conditions we lower first the order of equation by applying integration by parts on the second-order derivative term and then we apply a similar procedure

$$R_i^4 = -\int_{r_a}^{r_0} \left[a \left[\frac{\partial p}{\partial r} \right]^{n+1} + (1-a) \left[\frac{\partial p}{\partial r} \right]^n \right] \frac{\partial \Phi^i}{\partial r} \, \mathrm{d}r + \int_{r_a}^{r_0} \left\{ a \left[\frac{1}{r} + \frac{3-\phi^{n+1}}{\phi^{n+1}(1-\phi^{n+1})} \left[\frac{\partial \phi}{\partial r} \right]^{n+1} - \frac{\rho_{\mathrm{s}} - \rho_{\mathrm{f}}}{(1-c^{n+1})\rho_{\mathrm{f}} + c^{n+1}\rho_{\mathrm{s}}} \left[\frac{\partial c}{\partial r} \right]^{n+1} \right] \times \left[\frac{\partial p}{\partial r} \right]^{n+1} + (1-a) \left[\frac{1}{r} + \frac{3-\phi^n}{\phi^n(1-\phi^n)} \left[\frac{\partial \phi}{\partial r} \right]^n - \frac{\rho_{\mathrm{s}} - \rho_{\mathrm{f}}}{(1-c^n)\rho_{\mathrm{f}} + c^n\rho_{\mathrm{s}}} \left[\frac{\partial c}{\partial r} \right]^n \right] \times \left[\frac{\partial p}{\partial r} \right]^n \right\} \Phi^i \, \mathrm{d}r \tag{46}$$

The (i-th row, j-th column) element of Jacobian is

$$\frac{\partial R_i^1}{\partial \phi} = \int_{r_a}^{r_0} \left[\frac{c}{\Delta t} \Phi^i \Phi^j - \frac{1}{\Delta t} \Phi^i \Phi^j \right] \mathrm{d}r \tag{47}$$

$$\frac{\partial R_i^1}{\partial c} = \int_{r_a}^{r_0} \left[\frac{\phi}{\Delta t} \Phi^i \Phi^j - aq\Phi^i \frac{\partial \Phi^j}{\partial r} \right] \mathrm{d}r \tag{48}$$

$$\frac{\partial R_i^1}{\partial q} = \int_{r_a}^{r_0} - a \frac{\partial c}{\partial r} \Phi^i \Phi^j \, \mathrm{d}r \tag{49}$$

$$\frac{\partial R_i^2}{\partial \phi} = \int_{r_a}^{r_0} \left[\frac{1}{\Delta t} \Phi^i \Phi^j + a\lambda' \left(c - \frac{c^2}{c_{\mathrm{cr}}} \right) q \Phi^i \Phi^j \right] \mathrm{d}r \tag{50}$$

$$\frac{\partial R_i^2}{\partial c} = \int_{r_a}^{r_0} - a\lambda'(1-\phi) \left(1 - \frac{2c}{c_{\mathrm{cr}}} \right) q \Phi^i \Phi^j \, \mathrm{d}r \tag{51}$$

$$\frac{\partial R_i^2}{\partial q} = \int_{r_a}^{r_0} - a\lambda'(1-\phi) \left(c - \frac{c^2}{c_{\mathrm{cr}}} \right) \Phi^i \Phi^j \, \mathrm{d}r \tag{52}$$

$$\frac{\partial R_i^3}{\partial \phi} = \int_{r_a}^{r_0} \left[a \frac{\eta_{\mathrm{k}}}{k_0} \frac{\phi^2 - 4\phi + 3}{\phi^4} \bar{\rho} q \right] \Phi^i \Phi^j \, \mathrm{d}r \tag{53}$$

$$\frac{\partial R_i^3}{\partial c} = - \int_{r_a}^{r_0} \left[a \frac{\eta_{\mathrm{k}}}{k_0} \frac{(1-\phi)^2}{\phi^3} (\rho_{\mathrm{s}} - \rho_{\mathrm{f}}) q \right] \Phi^i \Phi^j \, \mathrm{d}r \tag{54}$$

$$\frac{\partial R_i^3}{\partial q} = - \int_{r_a}^{r_0} \left[a \frac{\eta_{\mathrm{k}}}{k_0} \frac{(1-\phi)^2}{\phi^3} \bar{\rho} \right] \Phi^i \Phi^j \, \mathrm{d}r \tag{55}$$

$$\frac{\partial R_i^3}{\partial p} = \int_{r_a}^{r_0} a \frac{\partial \Phi^j}{\partial r} \Phi^i \, \mathrm{d}r \tag{56}$$

$$\frac{\partial R_i^4}{\partial \phi} = \int_{r_a}^{r_0} a \frac{\partial p}{\partial r} \left[\frac{3-\phi}{\phi(1-\phi)} \frac{\partial \Phi^j}{\partial r} - \frac{\phi^2 - 6\phi + 3}{\phi^2 (1-\phi)^2} \frac{\partial \phi}{\partial r} \Phi^j \right] \Phi^i \, \mathrm{d}r \tag{57}$$

$$\frac{\partial R_i^4}{\partial c} = \int_{r_a}^{r_0} - a \frac{\partial p}{\partial r} \left[\frac{\rho_{\mathrm{s}} - \rho_{\mathrm{f}}}{(1-c^{n+1})\rho_{\mathrm{f}} + c^{n+1}\rho_{\mathrm{s}}} \frac{\partial \Phi^j}{\partial r} - \frac{(\rho_{\mathrm{s}} - \rho_{\mathrm{f}})^2}{[(1-c^{n+1})\rho_{\mathrm{f}} + c^{n+1}\rho_{\mathrm{s}}]^2} \frac{\partial c}{\partial r} \Phi^j \right] \Phi^i \, \mathrm{d}r \tag{58}$$

$$\frac{\partial R_i^4}{\partial q} = \int_{r_a}^{r_0} \left[-a \frac{\partial \Phi^j}{\partial r} \frac{\partial \Phi^i}{\partial r} + a \frac{\partial \Phi^j}{\partial r} \Phi^i \left[\frac{1}{r} + \frac{3-\phi}{\phi(1-\phi)} \frac{\partial \phi}{\partial r} - \frac{\rho_{\mathrm{s}} - \rho_{\mathrm{f}}}{(1-c^{n+1})\rho_{\mathrm{f}} + c^{n+1}\rho_{\mathrm{s}}} \frac{\partial c}{\partial r} \right] \right] \mathrm{d}r \tag{59}$$

APPENDIX II

Discretization of stress equilibrium equation

The Galerkin-weighted residuals of stress equilibrium equation (32) are formed following a similar procedure.[13] The Galerkin form is first obtained by multiplying equation (32) with each basis function (Hermite cubic polynomials). Then the boundary conditions can be applied by lowering the order of equation and finally, the residuals are derived by integrating over the entire space-domain $[r_a, r_0]$,

$$R_i = \left[\Phi^i \frac{\partial u}{\partial r} \right]_{r_a}^{r_0} + \int_{r_a}^{r_0} \left[-\frac{\partial \Phi^j}{\partial r} \frac{\partial u}{\partial r} + \Phi^i \frac{\partial u}{\partial r} g_1(r) - \Phi^i g_2(r) - \Phi^i g_3(r) \frac{\partial (\phi p)}{\partial r} \right] \mathrm{d}r \tag{60}$$

with

$$\begin{aligned} g_1(r) &= \frac{1}{r} - \frac{1}{1-\phi} \frac{\partial \phi}{\partial r} \\ g_2(r) &= \frac{1}{r^2} + \frac{1}{r} \frac{v}{1-v} \frac{1}{1-\phi} \frac{\partial \phi}{\partial r} \\ g_3(r) &= \frac{(1+v)(1-2v)}{\bar{E}(1-\phi)(1-v)} \end{aligned} \tag{61}$$

Equation (41) can be written in the following form:

$$a_{ij} u_j = b_i \tag{62}$$

where the matrix coefficients are given by

$$a_{ij} = \int_{r_a}^{r_0} \left[-\frac{\partial \Phi^j}{\partial r} \frac{\partial \Phi^i}{\partial r} + \Phi^i \frac{\partial \Phi^j}{\partial r} g_1(r) - \Phi^i \Phi^j g_2(r) \right] \mathrm{d}r, \quad i = 1, \ldots, N, \; j = 1, \ldots, N \tag{63}$$

$$a_{11} = a_{11} + \frac{v}{1-v} \frac{1}{r_a}, \qquad a_{N-1,N-1} = a_{N-1,N-1} - \frac{v}{1-v} \frac{1}{r_0} \tag{64}$$

and

$$b_i = \int_{r_a}^{r_0} \left[\Phi^i g_3(r) \frac{\partial \phi p}{\partial r} \right] \mathrm{d}r, \quad i = 1, \ldots, N \tag{65}$$

$$b_1 = b_1 + \frac{(1+v)(1-2v)}{\bar{E}(1-v)} p_a, \qquad b_{N-1} = b_{N-1} - \frac{(1+v)(1-2v)}{\bar{E}(1-\phi_0)(1-v)} (\phi_0 p_0 - \sigma_0) \tag{66}$$

Finally, all the involved integrals were evaluated numerically using Gaussian integration.

REFERENCES

1. I. Vardoulakis, M. Stavropoulou and P. Papanastasiou, 'Hydromechanical aspects of sand production problem', *Transport in Porous Media*, **22,** 225–244 (1996).
2. P. Papanastasiou and I. Vardoulakis, 'Numerical treatment of progressive localization in relation to borehole stability', *Int. J. Numer. Anal. Meth. Geomech.*, **16,** 389–424 (1992).

3. M. G. A. Veeken, D. R. Davies, C. J. Kenter and A. P. Kooijman, 'Sand production review: developing an integral approach', *SPE 22792*, 335–346 (1991).
4. I. Bradford and J. Cook, 'A semi-analytic elastoplastic model for wellbore stability with applications to sanding', *Eurock'94*, *Balkema*, 347–353 (1994).
5. J. Tronvoll and F. Fjaer, 'Experimental study of sand production from perforation cavities', *Int. J. Rock Mech. Min. Sci. Geomech. Abstr.*, **31**(5), 393–410 (1994).
6. R. Sakthivadivel, 'Theory and mechanism of filtration of non-colloidal fines through a porous medium', HEL 15-5,6,7, University of California, Berkekey, 1966.
7. R. Sakthivadivel and S. Irmay 'A review of filtration theories', HEL 15-4, University of California, Berkekey, 1966.
8. I. Vardoulakis and J. Sulem, *Bifurcation Analysis in Geomechanics*, Blackie, London, 1995.
9. J. Lemaitre, *A Course on Damage Mechanics*, Springer, Berlin.
10. R. A. Plumb, 'Influence of composition and texture on the failure properties of clastic rocks' *Eurock'94*, 13–20. Balkema Rotterdam, 1994.
11. A. E. H. Love, *A Treatise on the Mathematical Theory of Elasticity*, Dover Publications, New York, 1944.
12. J. Bear, *Dynamics of Fluids In Porous Media*, Dover Publications, New York, 1988.
13. G. Strang G and G. J. Fix, *An Analysis of the Finite Element Method*, Prentice-Hall, Englewood Cliffs, NJ, 1973.

